REPORT DOCUMENTATION PAGE

Form Approved
OMB No. 0704-0188

1. REPORT DATE *(DD-MM-YYYY)*	2. REPORT TYPE	3. DATES COVERED *(From - To)*
	Technical Papers	

4. TITLE AND SUBTITLE

Please see attached

5a. CONTRACT NUMBER

5b. GRANT NUMBER

5c. PROGRAM ELEMENT NUMBER

6. AUTHOR(S)

5d. PROJECT NUMBER
2303

5e. TASK NUMBER
M2C8

5f. WORK UNIT NUMBER
345709

7. PERFORMING ORGANIZATION NAME(S) AND ADDRESS(ES)

Air Force Research Laboratory (AFMC)
AFRL/PRS
5 Pollux Drive
Edwards AFB CA 93524-7048

8. PERFORMING ORGANIZATION REPORT

9. SPONSORING / MONITORING AGENCY NAME(S) AND ADDRESS(ES)

Air Force Research Laboratory (AFMC)
AFRL/PRS
5 Pollux Drive
Edwards AFB CA 93524-7048

10. SPONSOR/MONITOR'S ACRONYM(S)

11. SPONSOR/MONITOR'S NUMBER(S)
Please see attached

12. DISTRIBUTION / AVAILABILITY STATEMENT

Approved for public release; distribution unlimited.

13. SUPPLEMENTARY NOTES

14. ABSTRACT

20030129 210

15. SUBJECT TERMS

16. SECURITY CLASSIFICATION OF:			17. LIMITATION OF ABSTRACT	18. NUMBER OF PAGES	19a. NAME OF RESPONSIBLE PERSON
					Leilani Richardson
a. REPORT	b. ABSTRACT	c. THIS PAGE	A		19b. TELEPHONE NUMBER *(include area code)*
Unclassified	Unclassified	Unclassified			(661) 275-5015

MEMORANDUM FOR PRS (Contractor Publication)

FROM: PROI (STINFO) 03 Apr 2001

SUBJECT: Authorization for Release of Technical Information, Control Number: **AFRL-PR-ED-TP-2001-074**
Simon Tam; Mario Fajardo, "Single and Double Infrared Transitions in Rapid Vapor Deposited Parahydrogen Solids: Application to Sample Thickness Determination and Quantitative Infrared Absorption Spectroscopy"

Peer Review Journal **(Statement A)**
(Deadline: N/A)

1. This request has been reviewed by the Foreign Disclosure Office for: a.) appropriateness of distribution statement, b.) military/national critical technology, c.) export controls or distribution restrictions, d.) appropriateness for release to a foreign nation, and e.) technical sensitivity and/or economic sensitivity.
Comments:_____

Signature _____ Date _____

2. This request has been reviewed by the Public Affairs Office for: a.) appropriateness for public release and/or b) possible higher headquarters review.
Comments: _____

Signature _____ Date _____

3. This request has been reviewed by the STINFO for: a.) changes if approved as amended, b) appropriateness of references, if applicable; and c.) format and completion of meeting clearance form if required
Comments:_____

Signature _____ Date _____

4. This request has been reviewed by PR for: a.) technical accuracy, b.) appropriateness for audience, c.) appropriateness of distribution statement, d.) technical sensitivity and economic sensitivity, e.) military/ national critical technology, and f.) data rights and patentability
Comments:_____

APPROVED/APPROVED AS AMENDED/DISAPPROVED

_____

PHILIP A. KESSEL Date
Technical Advisor
Space and Missile Propulsion Division

Single and Double Infrared Transitions in Rapid Vapor Deposited Parahydrogen Solids: Application to Sample Thickness Determination and Quantitative Infrared Absorption Spectroscopy

Simon Tam[a] and Mario E. Fajardo[b]
Propulsion Directorate, US Air Force Research Laboratory
AFRL/PRSP, Bldg. 8451, Edwards AFB, CA 93524-7680

[a] present address: KLA-Tencor Corp., 1 Technology Drive, Milpitas, CA 95035
[b] email: mario.fajardo@edwards.af.mil

Submitted to Rev. Sci. Instrum. _____, Received _____, Accepted _____

ABSTRACT

We present a convenient method for determining the thickness of a cryogenic parahydrogen (pH_2) solid from its infrared (IR) absorption spectrum. Millimeters-thick pH_2 solids of exceptional optical clarity can be produced by the rapid vapor deposition method [M.E. Fajardo and S. Tam, J. Chem. Phys. **108**, 4237 (1998)]. Doping of these pH_2 solids is readily accomplished by co-deposition of the desired impurities, making them excellent hosts for high-resolution matrix isolation spectroscopy. The intensities of the IR "double" transitions $Q_1(0)+S_0(0)$ and $S_1(0)+S_0(0)$ of the pH_2 host are insensitive to the matrix microstructure and to the presence of dopants, so these absorptions are especially well suited for thickness determinations. We calibrate the integrated absorption intensities of these two bands against the sample thicknesses determined from transmission interference fringes appearing in the same experimental spectra; we report: $\tilde{\alpha}[Q_1(0)+S_0(0)] = 4.84(\pm0.13)\times10^{-14}$ cm^3/s, and $\tilde{\alpha}[S_1(0)+S_0(0)] = 0.35(\pm0.02)\times10^{-14}$ cm^3/s (95% confidence). We also discuss several other advantages of rapid vapor deposited pH_2 solids as hosts for quantitative IR absorption spectroscopy of dopant species.

I. INTRODUCTION

We recently reported the production of millimeters-thick parahydrogen (pH_2) solids of exceptional optical clarity by rapid vapor deposition of pre-cooled pH_2 gas onto a liquid helium (lHe) cooled substrate.[1,2] Our sample-in-vacuum geometry permits the facile doping of these pH_2 solids with a variety of atomic and molecular, charged and neutral species[1-8] which we interrogate via matrix isolation spectroscopy (MIS). This work is part of the U.S. Air Force's High Energy Density Matter (HEDM) program;[9] our goal is to demonstrate practical chemical energy storage in cryogenic solids, and ultimately to use these materials as advanced rocket propellants.

Of more general interest are the advantages of using solid pH_2 as a host for MIS over the traditionally employed rare gas solids (RGS). High resolution ($\Delta\nu/\nu < 10^{-6}$) infrared (IR) vibrational absorption spectroscopy in solid pH_2 was first demonstrated by Oka and co-workers at the U. of Chicago in the 1980's,[10] and further developed in collaboration with the group of Shida and Momose at Kyoto U.[11,12] The relatively "soft" nature of the pH_2 host[10,12] and the typically weaker guest-host interactions, reduce the occurrence and importance of trapping site inhomogeneities, resulting in the observed sharp absorptions. The correspondingly reduced cage effect in solid pH_2 allows for more efficient production of novel chemical species by *in-situ* photolysis or radiolysis,[12,13] and suggests a myriad of possibilities for studying condensed phase chemical processes in a minimally perturbing environment. Furthermore, foreign dopant species induce weak but measurable IR activity in the neighboring pH_2 molecules; thus, in addition to the direct IR absorptions of the dopant "solute," a single IR spectrum contains information about the response of the pH_2 "solvent," as well.[1] Growing recognition of these advantages is resulting in an increasing popularity of solid pH_2 as a host for MIS studies.

Another advantage of utilizing solid pH_2 as a host for MIS that has received little explicit mention to date is its special suitability for quantitative absorption spectroscopy. By this we mean the facile application of Beer's Law[14] to determine absolute dopant concentrations from experimental absorption spectra. This is of obvious importance to our HEDM chemical energy storage effort, as well as to other analytical applications of MIS.[15] For experimental decadic absorbance spectra recorded as a function of wavenumber, $\tilde{\nu}$ (cm^{-1}):

$$A(\tilde{\nu}) = -\log_{10}\left[\frac{I(\tilde{\nu})}{I_0(\tilde{\nu})}\right] \tag{1}$$

we state Beer's Law as:

$$A(\tilde{\nu}) = \frac{1}{2.303}\sum_X \alpha_X(\tilde{\nu})\, C_X\, d \tag{2}$$

in which: $\alpha_X(\tilde{\nu})$ is a molecular absorption coefficient (cm^2/mol), C_X is the concentration (mol/cm^3) of species X, and d is the sample thickness (cm). Alternative definitions and units systems are also in common usage.[16,17] For spectrally isolated absorption bands, the dopant concentrations are most accurately calculated via the related expression:

$$C_X = \frac{2.303\int_{band} A\,(\tilde{\nu})\, d\tilde{\nu}}{d\int_{band}\alpha_X(\tilde{\nu})\, d\tilde{\nu}} \tag{3}.$$

We also routinely report fractional dopant concentrations normalized by:

$$X\,\% = 100\%\left(\frac{C_X N_A}{N_{host}}\right) \tag{4}$$

or

$$X\,(ppm) = 10^6\left(\frac{C_X N_A}{N_{host}}\right) \tag{5}$$

in which: $N_A = 6.022 \times 10^{23}$ #/mol is Avogadro's constant, and N_{host} is the number density of the matrix host ($N_{pH2} = 2.60 \times 10^{22}$ #/cm^3 at lHe temperatures, ref. 18).

Several favorable properties of rapid vapor deposited pH_2 solids contribute to the straightforward evaluation and accurate application of these expressions. Their extreme optical clarity eliminates troublesome sloping spectral baselines usually encountered in thick rare gas matrices due to wavelength dependent scattering losses. The (often) sharp dopant spectral features further facilitate the determination of absorption band integration limits and baselines. The millimeters-long useful optical pathlengths and sharp dopant spectral features combine to permit the facile detection of many dopants at very low (~ 1 ppm) concentrations, which eliminates "deviations" from Beer's Law due to dopant-dopant interactions (conversely, dopant aggregation and other "intermolecular interactions" can be studied systematically by increasing concentrations from this well isolated limit). Analysis of the condensed-phase induced IR absorptions of the host pH_2 molecules[19-28] demonstrates that the as-deposited pH_2 hosts are close-packed solids with a mixed hexagonal close-packed (hcp) and face-centered cubic (fcc) polycrystalline microstructure,[1,4] and that the metastable fcc regions largely anneal away[1,4,5,7,8] upon warming above $T \approx 4.5$ K. Thus, these samples are neither amorphous nor porous; instead, they have very nearly the same bulk density as pH_2 solids grown from the melt. As we will show below, the pH_2 absorptions also conveniently permit determination of the sample thickness from the same spectral data containing the dopant absorption features, ensuring that they relate to the same experimental interrogation volume. Finally, the low index of refraction of solid pH_2 implies only weak perturbations to the absolute intensities of dopant vibrational transitions,[29-37] reducing the magnitude of the errors associated with this correction. This last point deserves a

brief further discussion.

For IR absorptions occurring in condensed phases, the electromagnetic field experienced by the absorbing molecule is modified by the dielectric properties of the host. Many models of the consequences of this "effective" or "local" field to experimental observables have been proposed.[29-37] In particular, the so-called "Chako" or "Polo-Wilson" equation[29,30] can be used to correct the molecular absorption coefficients:

$$\alpha_X^{matrix} = \alpha_X^{gas} \frac{1}{n}\left(\frac{n^2+2}{3}\right)^2 \qquad (6)$$

in which n is the index of refraction of the matrix host. Disagreement persists to date on which "index of refraction" should be used in Eqn. (6); e.g.: should it include any frequency dependence, or contributions from the dopant molecule, etc. For our purposes we take:

$$n = n_0 = \sqrt{\varepsilon_0} \qquad (7)$$

in which: n_0 and ε_0 are the DC (zero frequency) refractive index and dielectric constant of the matrix host, respectively. For solid pH_2 at lHe temperatures $\varepsilon_0 = 1.297$ (refs. 38-40); thus $n_{pH2} = 1.14$, and $\alpha_X^{pH2} = 1.06\ \alpha_X^{gas}$. For comparison, the refractive index of a solid Ar matrix is $n_{Ar} = 1.29$ (ref. 41), resulting in a significantly larger gas-to-matrix correction of: $\alpha_X^{Ar} = 1.16\ \alpha_X^{gas}$.

In what follows we describe our approach for determining the thickness of a pH_2 solid from the condensed-phase induced IR absorptions of the host pH_2 molecules. We will present data gathered from MIS experiments on over 100 different pure and doped pH_2 samples. We will show that the so-called "double" $Q_1(0)+S_0(0)$ and $S_1(0)+S_0(0)$ transitions,[42] in which a pair of nearest neighbor pH_2 molecules cooperate to absorb a single photon,[19-28] are well suited for thickness determinations. We point out possible pitfalls to using "single" transitions, such as the

$S_1(0)$ or $U_0(0)$ bands, for this purpose. We provide recommended spectral integration regions and baselines, and corresponding calibration factors based on a comparison with interferometrically determined sample thicknesses. We conclude with example concentration calculations for a CO_2 doped pH_2 solid.

II. EXPERIMENTAL

Our experimental apparatus and techniques have been described before;[1-8] here we give only a brief review of our previous descriptions, and focus instead on aspects relevant to quantitative spectroscopic measurements.

A. Apparatus

Fig. 1 shows a section view through the center of the deposition chamber of our lHe bath cryostat. The octagonal vacuum shroud measures 7.62 cm across the flats; eight o-ring sealed ports allow for sample preparation and optical access. The chamber sits directly atop a small (30 l/s) turbomolecular pump which provides a room temperature vacuum ~ 10^{-7} Torr.

Solid pH_2 samples are prepared by deposition onto a 0.4 cm-thick, 0.5°-wedged BaF_2 substrate clamped in a gold-plated oxygen free high conductivity (OFHC) copper holder which is cooled by the lHe reservoir; all thermal connections are made with 100 μm-thick indium foil. The deposition substrate is surrounded by a liquid nitrogen (lN_2) cooled aluminum radiation shield in which openings are cut for sample preparation and optical access. Operating the ortho/para H_2 converter[2] at T =15 K yields a flow of pre-cooled pH_2 gas containing ~ 0.01 % residual ortho-H_2 and ~ 0.03 % HD (assuming natural isotopic abundance) and only sub-ppm

concentrations of condensable impurities. This cold, purified pH_2 gas is delivered to the BaF_2 substrate through a thin wall brass tube oriented at a 45° angle to the substrate surface normal; the tube terminates about 3 cm from the center of the sample substrate. Because of the sample-in-vacuum design of our cryostat, during a deposition the cryogenic thermal isolation vacuum must be maintained below ~ 10^{-4} Torr of uncondensed H_2 gas to avoid thermal runaway. An independent flow of dopant species produced by any of a variety of standard methods[2] can be readily co-deposited with the pH_2 gas.

The majority of the pH_2 gas freezes to form a curved solid deposit on the "front" side of the sample substrate and holder, depicted schematically in Fig. 1. The uncondensed pH_2 gas results in the deposition of a second solid H_2 film on the "back" side of the BaF_2 substrate. We will show below that for our aparatus this back side deposit amounts to 8.7 % of the main front side sample thickness, and that this 11.5:1 front:back thickness ratio is roughly independent of the pH_2 inlet flow rate over the 1 to 60 mmol/hr range. The amount of pH_2 gas which "misses" the sample substrate can be controlled by adjusting the position of the brass inlet tube: moving the end of this tube closer to the substrate results in more efficient pH_2 deposition, but also in a more strongly curved front side deposit.

The IR absorption spectra of the pH_2 solids used to calibrate our sample thickness determinations are obtained along the main optical axis with a Fourier transform infrared (FTIR) spectrometer (Mattson Nova Cygni 120) capable of 0.09 cm^{-1} resolution, which simultaneously probes both front and back side pH_2 samples. We employ a glowbar source, a Ge coated KBr beamsplitter, and an lN_2 cooled HgCdTe detector (16 μm long-wavelength cut-off) to obtain interferograms which we Fourier transform (triangle apodization, Mertz phase correction) into

spectra over a usable range of 800 to 5400 cm^{-1}. To accommodate the IR diagnostic the cryostat and IR optics reside inside a 0.5 m^3 polycarbonate box purged with a constant flow of dry N_2 gas.

During some depositions we also monitor the sample growth by back-reflection interferometry using a HeNe laser beam incident along the optical axis ($\theta = 0$):[43,44]

$$d = \frac{m \lambda_{HeNe}}{2 n \cos(\theta)} \tag{8}$$

in which: d is the pH_2 sample thickness, m is the number of fringes, $\lambda_{HeNe} = 0.633$ μm is the HeNe laser wavelength, and we take the index of refraction $n = n_{pH2} = 1.14$.

We also present recently recorded absorption spectra of a CO_2/pH_2 sample obtained with a Bruker IFS120HR FTIR spectrometer using a Ge coated KBr beamsplitter and two source/detector combinations: a glowbar source and a different lN_2 cooled HgCdTe detector (18 μm long-wavelength cut-off), and a tungsten filament source combined with an lN_2 cooled InSb detector.

B. Analysis of Spectrometric Errors

The wedged shape of the front side solid pH_2 deposit can, in principle, introduce spectrometric errors, $\delta A(\tilde{\nu})$, into our absorption measurements:[45]

$$\delta A(\tilde{\nu}) \approx \frac{1}{10} [A(\tilde{\nu})]^2 \left(\frac{\Delta d}{d}\right)^2 \tag{9}$$

where Δd is the thickness variation across the sample observation volume; however, we show here that under our experimental conditions such errors are negligible. We assume that the pH_2 flux from the brass inlet tube, and hence the deposited sample thickness, can be approximated for small angles ϕ by:[46]

$$\Phi_{pH2}(\phi,r) \propto \frac{\cos^2(\phi)}{r^2} \qquad (10)$$

where ϕ and r are measured from the centerline and the open end of the inlet tube, respectively. The front side pH_2 deposit depicted in Fig. 1 is drawn assuming the validity of Eqn. (10) and a constant pH_2 sticking probability; the shape compares well with visual observations. We focus the IR probe beam to a 3 mm diameter (or smaller) spot at the sample, yielding an upper limit of $\Delta d/d \approx 0.09$ and $\delta A(\tilde{\nu}) \approx 8x10^{-4} [A(\tilde{\nu})]^2$, which we disregard for $A(\tilde{\nu}) < 1$.

Our use of photoconductive HgCdTe IR detectors raises the possibility of spectrometric errors originating from (overdriven) detector nonlinearities.[14,47,48] These nonlinearities primarily influence the strong centerburst region of the interferogram, which Fourier transforms into distortions of the spectral baseline. Indeed, inspection of typical single-beam $I_0(\tilde{\nu})$ spectra from both the Mattson and Bruker FTIR systems reveals false non-zero intensities at wavenumbers below the ≈ 700 cm^{-1} BaF_2 window cut-off, confirming our operation of these detectors in overdriven IR intensity regimes. This problem is partially mitigated by the fact that in any given MIS experiment the combination of pH_2 sample absorption and reduced Fresnel reflection losses at the BaF_2 substrate-to-vacuum interfaces modify the total intensity of the IR beam by less than $\pm$ 10 %, so the detector must follow the centerburst signal over only this modest range. Numerical correction for the resulting baseline distortions is complicated by the partial compensation for detector nonlinearities which occurs during the phase correction stage of the FT process.[48] Instead of attempting any such theoretical corrections, we present the results of additional experiments with the same Mattson FTIR system in order to quantify the systematic errors arising from detection nonlinearity. We will present the absorption spectra from the Bruker FTIR system without performing a separate independent evaluation of nonlinear errors.

To this end we measure IR absorption spectra of a nominal 5 % $CHCl_3/CCl_4$ solution held in a 0 to 0.6 cm variable pathlength cell (Specac 7500) equipped with non-rotating KRS-5 windows. Single-beam spectra of the cell filled with CCl_4 (obtained at each pathlength) constitute the $I_0(\tilde{\nu})$ data. We calibrate the cell's length scale experimentally from the pattern of transmission interference fringes in IR spectra of the empty cell at several pathlengths, d:[14]

$$d = \frac{m}{2\, n \cos(\theta)\, [\tilde{\nu}_1 - \tilde{\nu}_2]} \tag{11}$$

in which: $\theta = 0$ for normal incidence, $n = 1.0003$ is the index of refraction of air, and m is the number of fringes observed over the $\tilde{\nu}_1 - \tilde{\nu}_2$ wavenumber range. We estimate our absolute pathlength errors as ± 0.001 cm. We adjust the IR intensity at the HgCdTe detector, and focus our attention to the 4000 to 4500 cm^{-1} region, in order to reproduce as closely as possible the same overdriven detector conditions as encountered during the pH_2 experiments. During these experiments the $CHCl_3$ absorptions and mechanical cell replacement errors result in about ± 10 % variations in the centerburst intensities between $I_0(\tilde{\nu})$ and $I(\tilde{\nu})$ measurements.

The top panel of Fig. 2 shows a correlation plot of the integrated intensity of the $\nu_1+\nu_4$ $CHCl_3$ absorption[49] vs. sample pathlength, along with the best fit linear (dotted trace) and quadratic (solid trace) polynomials:

$$\int A(\tilde{\nu})\, d\tilde{\nu} \equiv y = a_0 + a_1 d \tag{12a}$$

$$= b_0 + b_1 d + b_2 d^2 \tag{12b}$$

with parameter values: $a_0 = 0.3142\ cm^{-1}$, $a_1 = 51.73\ cm^{-2}$, $b_0 = -0.0747\ cm^{-1}$, $b_1 = 54.98\ cm^{-2}$, and $b_2 = -5.041\ cm^{-3}$. We note that for d = 0.573 cm, the peak absorbance is $A(4214\ cm^{-1}) = 0.865$, so we can ultimately generalize our results from pathlength to peak absorbance in the neighborhood

of $\tilde{\nu} \approx 4200$ cm^{-1} by the substitution: $d = 1$ cm $\rightarrow A(\tilde{\nu}) = 1.51$.

At first glance the data seem to fall right on the straight line, but closer inspection reveals systematic deviations which justify the use of a quadratic fit. The negative value of the b_2 coefficient denotes the negative curvature consistent with a mild saturation of the detection response over this range of absorbances. The close approach by the fitted quadratic curve to the origin and the uniform distribution of the residuals in the bottom panel of Fig. 2 confirm that this fit adequately describes our data.

Recalling Eqn. (3), the quantity of interest in our measurements is the quotient y/d, which would be equal to the slope, y′, of the y vs. d correlation plot in the absence of nonlinearities. In practice, the slope extracted from a linear fit includes an error which we can estimate using the parameters of the quadratic fit. The slope of a line tangent to the quadratic fit curve at any given pathlength is:

$$y' = b_1 + 2b_2 d \qquad (13).$$

By numerical comparison we find that, for the data in Fig. 2, the slope of the best straight line fit over some range $0 < d < d_{max}$ is approximately equal to the slope of the line tangent to the quadratic fit at $d_{avg} = d_{max}/2$. Thus, we can estimate the fractional systematic error in the slope of a best fit straight line as a function of maximum pathlength or peak absorbance as:

$$\frac{\delta y'}{y'} \approx \frac{b_2 d_{max}}{b_1} = -0.09\, d_{max} = -0.06\, A_{max}(\tilde{\nu}) \qquad (14).$$

As expected, the fractional error in the fitted slope increases for thicker samples and higher peak absorbances. We will use Eqn. (14) below to estimate the magnitudes of systematic nonlinear errors in our pH_2 experiments.

III. RESULTS AND DISCUSSION

A. Single and Double IR Transitions

In pure solid pH_2, infrared activity in the homonuclear diatomic H_2 molecules arises from dipole moments induced by intermolecular interactions with neighboring pH_2 molecules.[19-28] An especially helpful and succinct summary of the observed IR transitions and their underlying physical mechanisms can be found in ref. 24. Very briefly: the "single" and "double" absorptions are zero-phonon lines involving the ro-vibrational degrees of freedom of one pH_2 molecule, or a pair of pH_2 molecules, respectively. Of special importance here is the fact that the interactions responsible for single transitions are subject to a symmetry-dependent "cancellation effect;" making their transition intensities very sensitive to the particular structures of the sites occupied by the pH_2 molecules. In contrast, for the double transitions (in which a pair of nearest neighbor pH_2 molecules share the energy from a single photon) the transition intensities are very insensitive to the symmetry of the surrounding pH_2 solid, and depend primarily on the solid's bulk density. In addition to these zero-phonon transitions, broad and typically strong phonon branches with long high-energy tails ("R-branches") are also observed.

Fig. 3 shows the sharp $S_1(0)$ line near 4486 cm^{-1}, and the associated broad $S_R(0)$ phonon band peaking near 4550 cm^{-1}, as well as the two double transitions which are the main focus of this manuscript: the $Q_1(0)+S_0(0)$ (4495 to 4520 cm^{-1}) and $S_1(0)+S_0(0)$ (4825 to 4855 cm^{-1}) bands. These double absorption features are not spectrally well-isolated from neighboring bands, so we arbitrarily choose the above listed wavenumber ranges as convenient band integration limits; the corresponding linear integration baselines are depicted in Fig. 3 as dotted line segments. We present data below demonstrating the relative merits of single and double transitions for the determination of solid pH_2 sample thicknesses.

Fig. 4 shows the effects of sample annealing on the intensity of the $S_1(0)$ feature for another rapid vapor deposited pH_2 solid. During the temperature cycle, the $S_1(0)$ line grows irreversibly, roughly doubling in integrated intensity; however, the integrated intensity of the $Q_1(0)+S_0(0)$ band (not shown) remains constant within ± 2 %. As mentioned above in the introduction, we have previously demonstrated[1,2,4,7,8] that our rapid vapor deposited pH_2 samples do not initially solidify into the thermodynamically stable hcp crystal structure obtained by slowly freezing liquid pH_2. Our as-deposited samples are neither amorphous nor porous, however any close packed structure such as hcp, or fcc, or conceivably even random-stacking of close packed planes (rcp) may be present. We have also previously shown that annealing of these pH_2 samples to above T ≈ 4.5 K irreversibly converts most of the non-hcp regions to hcp (however ~ 100 ppm concentrations of large dopants such as C_{60} can inhibit this transformation[5]). The presence of the $S_1(0)$ line in Figs. 3 and 4(a) requires that some of the pH_2 molecules initially reside in sites which lack a center of inversion,[21] i.e. in hcp regions or perhaps in locally "hcp-like" layers[5,7] within rcp regions. The irreversible growth of the $S_1(0)$ line shown in Fig. 4 is thus consistent with the permanent conversion of some or all of the non-hcp regions into hcp upon annealing. We observe similar annealing behavior for the $U_0(0)$ line near 1167 cm^{-1}. Thus, the variability of these single transitions with sample microstructure precludes their general use for determining the thicknesses of rapid vapor deposited pH_2 solids. In contrast to this behavior, the $Q_1(0)+S_0(0)$ and $S_1(0)+S_0(0)$ bands show good stability over the life of a ~ 0.1 cm-thick pH_2 sample, seldom varying by more than ± 5 % even after annealing at T = 4.8 K for 1 hour (however ~ 10 μm-thick samples can completely sublime away under these conditions). This is due to the fact that the various close packed structures share identical nearest neighbor

separations and bulk densities.

The stability of the intensities of the double transitions is further illustrated by Fig. 5, which shows a correlation plot of the integrated intensities of the $Q_1(0)+S_0(0)$ vs. $S_1(0)+S_0(0)$ bands, which we abbreviate as $\int A_{Q+S} d\tilde{\nu}$ and $\int A_{S+S} d\tilde{\nu}$, respectively. We note that Fig. 5 includes data from most of the pH_2 deposition experiments performed in our laboratory over a two-year period; we have only excluded data for which: $\int A_{Q+S} d\tilde{\nu} > 25$ cm^{-1}, or $\int A_{S+S} d\tilde{\nu} < 0.005$ cm^{-1}, or from spectra obtained at resolutions inferior to 1 cm^{-1}, or from spectra of highly scattering samples. The best fit straight line (constrained to pass through the origin, i.e.: $y = a_1 x$) has a slope of $a_1 = 13.18$ and seems to represent the data well, even for the thickest samples.

The success of this linear fit is somewhat surprising as we might reasonably expect the stronger $Q_1(0)+S_0(0)$ band to exhibit the effects of nonlinear detection sensitivity well before the weaker $S_1(0)+S_0(0)$ band, and so the plot might reasonably show some negative curvature. Specifically, the thickest samples depicted in Fig. 5 exhibit peak absorbances of $A_{max}(4510 \text{ cm}^{-1}) \approx 2.2$ and $A_{max}(4843 \text{ cm}^{-1}) \approx 0.17$, leading to expected fractional nonlinear errors from Eqn. (14) of - 13 % and - 1 %, respectively. No such curvature is obvious to the eye, perhaps being masked by the scatter in the data, moreover we are unable to detect any systematic deviations from linearity via numerical analysis of these data. For example, restricting the data sample set further to $\int A_{Q+S} d\tilde{\nu} < 12$ cm^{-1} and then to $\int A_{Q+S} d\tilde{\nu} < 5$ cm^{-1} yields fitted line slopes of $a_1 = 12.86$ and 12.91, respectively; if detection nonlinearities were significant we would expect larger, rather than smaller, a_1 values.

Fig. 6 shows these same 228 data recast as a histogram of the quotient $\int A_{Q+S} d\tilde{\nu} / \int A_{S+S} d\tilde{\nu}$. The mean value is $\mu = 13.04 \pm 0.08$ ($\pm$ the standard error of the mean[50]) and the sample standard

deviation is $\sigma = 1.22$, however comparison of the histogram with the normal distribution having the same μ and σ shows that the measured values are not normally distributed. Most of the outliers come from the thinnest samples; for example, restricting the data set to the 164 data with $\int A_{Q+S} d\tilde{\nu} > 5$ cm^{-1} yields $\mu = 13.02 \pm 0.06$ and $\sigma = 0.82$, and eliminates all values less than 10 and greater than 16. Conversely, restricting the data set to the 64 data with $\int A_{Q+S} d\tilde{\nu} < 5$ cm^{-1} yields $\mu = 13.09 \pm 0.24$ and $\sigma = 1.89$, so even the data from these thinnest samples show roughly the same mean value. We summarize our various efforts to analyze these data by stating that our best estimate for the quotient $\int A_{Q+S} d\tilde{\nu} / \int A_{S+S} d\tilde{\nu}$ is 13.0 ± 0.4 (95% confidence), and that the sample standard deviation is $\sigma = 1.2$. Since our analysis of these data do not reveal any effects of detection nonlinearity, we do not apply any correction for it.

B. Absolute Sample Thicknesses

We can estimate the absolute thicknesses of our pH_2 solids from the pattern of transmission interference fringes appearing in some IR spectra using Eqn. (11), or from fringes recorded by back-reflection HeNe laser interferometry during sample deposition using Eqn. (8), assuming in either case an index of refraction of $n = n_{pH2} = 1.14$. Recalling Fig. 1, our deposition method forms pH_2 solids on both the "front" and "back" sides of the BaF_2 substrate; we refer to their thicknesses as d_{front} and d_{back}, respectively, and to the total thickness of solid pH_2 in the optical path as $d_{total} = d_{front} + d_{back}$.

Fig. 7 shows IR spectra for three different pH_2 solids; the intensities of the pH_2 absorptions in the 4000 to 5000 cm^{-1} region help to sort out the evolution of the pattern of interference fringes with increasing total sample thickness. For very thin samples, $d_{total} < 20$ μm,

only the fringes from the front side film are apparent, as shown in Fig. 7(a); note also the strong wavelength dependent scattering losses typical of slowly deposited pH_2 solids. Fig. 7(b) shows a somewhat thicker sample which exhibits fringes from both the front and back side films; for such samples with 20 $\mu m < d_{total} < 70$ μm, we can simultaneously determine both d_{front} and d_{back} directly from the IR spectrum. For thicker samples the curvature of the front side deposit increases to the point that its transmission interference fringes disappear, leaving just the fringes from the back side solid, as shown in Fig. 7(c). Eventually, for even thicker samples with $d_{total} > 0.1$ cm, the fringes from the back side deposit also effectively disappear, leaving a conveniently smooth spectral baseline.

Fig. 8 shows the back reflection HeNe laser interference fringes recorded during the deposition of a Si/pH_2 sample. The inset shows the first two minutes of the deposition; during the first minute fringes due to the growth of both front and back side samples are apparent. The direct observation of fast and slow fringes in the back reflection measurements confirms our interpretation that the interference fringes in the IR spectra arise from front and back side films.

Fig. 9 shows a correlation plot of the integrated absorbance of the $Q_1(0)+S_0(0)$ transition vs. the interferometrically determined total pH_2 thickness, for all 11 samples for which both d_{front} and d_{back} can be determined simultaneously. The slope of the best fit straight line through the origin is $a_1 = 0.00821$ $cm^{-1}/\mu m$. The mean of the quotient $\int A_{Q+S} d\tilde{\nu} / d_{total}$, taken over these 11 data, is $\mu = 0.00822 \pm 0.00006$ $cm^{-1}/\mu m$; the sample standard deviation is $\sigma = 0.0002$ $cm^{-1}/\mu m$. For the thickest sample depicted in Fig. 9, the peak absorbance is $A_{max}(4510\ cm^{-1}) \approx 0.04$, resulting in a fractional nonlinear error from Eqn. (14) of - 0.4 %, or - 0.00003 $cm^{-1}/\mu m$. Thus, our recommended value is $\int A_{Q+S} d\tilde{\nu} / d_{total} = 0.0082 \pm 0.0002$ $cm^{-1}/\mu m$, or equivalently, 82 ± 2 cm^{-2}

(95% confidence). Finally, incorporating our best value for the quotient $\int A_{Q+S} d\tilde{\nu} / \int A_{S+S} d\tilde{\nu}$ we can estimate $\int A_{S+S} d\tilde{\nu} / d_{total} = 6.3 \pm 0.3$ cm^{-2} (95% confidence). These calculations are summarized in Table I.

C. Extrapolation to Thicker pH_2 Solids

We can extrapolate the correlation plot of $Q_1(0)+S_0(0)$ integrated absorbance vs. pH_2 sample thickness up to nearly 0.1 cm-thick samples by estimating d_{total} from our interferometric measurements of d_{back}. We obtain the ratio of the front:back sample thicknesses independently from the HeNe back reflection measurements and from the IR spectra of the 11 samples described in Fig. 9. We have available HeNe back reflection interference data from 30 pH_2 depositions; the mean of d_{front}/d_{back} over these data is $\mu = 11.4 \pm 0.2$, with a sample standard deviation of $\sigma = 0.8$. The 11 pH_2 samples for which the IR spectra reveal both d_{front} and d_{back} yield a mean d_{front}/d_{back} of $\mu = 12.3 \pm 0.4$, with a sample standard deviation of $\sigma = 1.2$. By trial and error we find that a value of $d_{front}/d_{back} = 11.5$ gives values of d_{total} in good agreement with the extrapolation of the $\int A_{Q+S} d\tilde{\nu} / d_{total} = 82$ cm^{-2} line, as shown in Fig. 10. In Fig. 10, the squares are data with d_{total} estimated as $d_{total} = (12.5/11.5)d_{front}$, and the triangles show values of d_{total} estimated as $d_{total} = 12.5 d_{back}$. Of course, this front:back thickness ratio is specific to this particular experimental setup. More important is the apparent absence of any significant curvature for solid pH_2 thicknesses approaching 0.1 cm.

With this reassurance, we can estimate the maximum useful thicknesses over which the $Q_1(0)+S_0(0)$ and $S_1(0)+S_0(0)$ double transitions can be used to determine pH_2 sample thicknesses. If we adopt the criterion $A_{max}(\tilde{\nu}) < 1$ to minimize nonlinear detection errors, then we can use the

$Q_1(0)+S_0(0)$ transition for d_{total} up to about 0.13 cm-thick pH_2 solids, and the $S_1(0)+S_0(0)$ transition for up to about 1.7 cm-thick solids:

$$d_{total}\ (cm) = \int A_{Q+S} d\tilde{\nu}\ (cm^{-1}) / 82\ (cm^{-2}) \tag{15a}$$

$$d_{total}\ (cm) = \int A_{S+S} d\tilde{\nu}\ (cm^{-1}) / 6.3\ (cm^{-2}) \tag{15b}.$$

Finally, we can estimate the thickness of the front side pH_2 deposit in our apparatus, which will contain any intentionally introduced dopant species, as:

$$d_{front} = (11.5/12.5)\ d_{total} \tag{16}.$$

D. Comparison with Literature Values

In the literature on the spectroscopy of pure molecular solids, two alternative forms of the integrated transition intensity are in regular use;[25] retaining symbols consistent with our previous definitions we have:

$$\tilde{\alpha} \equiv \frac{2.303\,c}{N_{pH2}\,d} \int_{band} A\ (\tilde{\nu})\ \frac{d\tilde{\nu}}{\tilde{\nu}} \tag{17}$$

in which: $c = 2.998 \times 10^{10}$ cm/s is the speed of light, and $\tilde{\alpha}$ has units of cm^3/s, and:

$$\alpha \equiv \frac{2.303}{d} \int_{band} A\ (\tilde{\nu})\ d\tilde{\nu} \tag{18}$$

in which α has units of cm^{-2}. This integrated transition intensity α is thus related to the integrated molecular absorption coefficient defined above in Eqn. (3) by:

$$\alpha = C_X \int_{band} \alpha_X(\tilde{\nu})\ d\tilde{\nu} = \frac{1}{V_m} \int_{band} \alpha_X(\tilde{\nu})\ d\tilde{\nu} \tag{19}$$

in which V_m is the host molar volume ($V_m[pH_2] = 23.2\ cm^3/mol$ at lHe temperatures, ref. 18). For reasonably sharp absorption bands:[25]

$$\tilde{\alpha} \approx \frac{\alpha c}{N_{pH2} < \tilde{\nu} >} \qquad (20)$$

where $< \tilde{\nu} >$ is the centroid of the absorption band. For the $Q_1(0)+S_0(0)$ and $S_1(0)+S_0(0)$ double transitions of interest here we take $< \tilde{\nu} >_{Q+S} = 4507$ cm^{-1} and $< \tilde{\nu} >_{S+S} = 4840$ cm^{-1}.

Table II shows a summary of our integrated transition intensity calculations, and lists the available literature experimental and theoretical values for comparison. Our value for $\tilde{\alpha}_{Q+S}$ and $\tilde{\alpha}_{S+S}$ are within ± 25 % of the previously published experimental values, however these deviations fall well outside our stated 95 % confidence limits. We note that the experimental literature values were obtained from spectra recorded using pH_2 sample thickness of 0.1 cm for the $Q_1(0)+S_0(0)$ transition,[19] and 2.6 cm for the $S_1(0)+S_0(0)$ transition.[24] We believe that our use of much thinner pH_2 samples helps to reduce systematic errors due to detection nonlinearities and other manifestations of the finite dynamic range of spectrometric apparatus.

E. Quantitative Absorption Spectroscopy

We conclude our discussion by presenting step-by-step sample calculations of the C and O atom isotopic abundances, and the absolute CO_2 dopant concentration derived from previously reported[7] spectra of a nominally 1.2 ppm CO_2/pH_2 sample. This serves as a definite example of the methods described above, documents the capabilities of our experimental apparatus, and illustrates certain issues peculiar to IR absorption spectroscopy in solid pH_2.

Fig. 11 shows the ν_3 absorptions of the $^{12}C^{16}O_2$ and $^{13}C^{16}O_2$ isotopomers at 0.008 cm^{-1} FWHM resolution, not shown is the ν_3 $^{12}C^{16}O^{18}O$ region near 2327 cm^{-1} in which similar features appear with a peak-to-peak S:N ratio of about 3:1. We record spectra at 0.008 cm^{-1} FWHM resolution using a glowbar source and a HgCdTe detector (40 co-added scans acquired in 0.79

hr), and at 0.05 cm^{-1} FWHM resolution using a tungsten filament source and an InSb detector (40 co-added scans acquired in 0.13 hr). The lower resolution data obtained with the more sensitive InSb detector show much better overall S:N ratios, however the 0.05 cm^{-1} resolution is not adequate to resolve the very sharp[7] CO_2 features. Inadequate spectral resolution can be an important source of spectrometric error in FTIR measurements,[14,47] and is an especially common pitfall when working with doped pH_2 solids.

From the high resolution HgCdTe spectra we extract: $\int A(\nu_3{}^{12}C^{16}O_2)d\tilde{\nu} = 0.1678$ cm^{-1}, $\int A(\nu_3{}^{13}C^{16}O_2)d\tilde{\nu} = 0.0019$ cm^{-1}, and $\int A(\nu_3{}^{12}C^{16}O^{18}O)d\tilde{\nu} = 0.0005$ cm^{-1}; using 3 cm^{-1}-wide integration regions of: 2343-2346 cm^{-1}, 2326-2329 cm^{-1}, and 2277.5-2280.5 cm^{-1}, respectively. The endpoints for linear integration baselines are obtained by averaging over 1 cm^{-1}-wide regions immediately adjacent to the integration regions, e.g.: 2342-2343 cm^{-1} and 2346-2347 cm^{-1} for the $^{12}C^{16}O_2$ region. We estimate the 95 % confidence limits for these integrations as ± 0.0004 cm^{-1} from comparable integrations of featureless portions of the 2200 to 2400 cm^{-1} region. These integrations yield spectroscopically measured isotopic abundances of: $^{12}C = 0.989 \pm 0.004$, $^{13}C = 0.011 \pm 0.002$, $^{16}O = 0.998 \pm 0.003$, and $^{18}O = 0.003 \pm 0.002$, in excellent agreement with the known[51] natural isotopic abundances: $^{12}C = 0.9890(3)$, $^{13}C = 0.0110(3)$, $^{16}O = 0.9976(1)$, and $^{18}O = 0.0020(1)$. Thus, the natural abundance isotopomers serve as convenient internal standards for testing the importance of nonlinear and other spectrometric errors; e.g.: the isotopic abundances extracted from the lower resolution InSb data show much larger deviations from the literature values.

However, the lower resolution and less noisy tungsten/InSb data are preferred for determining the thickness of the pH_2 solid host. Using the integration limits and baselines

depicted in Fig. 3 we extract integrated absorption intensities for the $Q_1(0)+S_0(0)$ and $S_1(0)+S_0(0)$ transitions of: $\int A_{Q+S} d\tilde{\nu} = 11.79$ cm^{-1} and $\int A_{S+S} d\tilde{\nu} = 0.932$ cm^{-1}, respectively. Applying Eqn. (15a) and Eqn. (15b) yields values of $d_{total} = 0.144 \pm 0.004$ cm and $d_{total} = 0.148 \pm 0.007$ cm, respectively. As these thicknesses are a little larger than the 0.13 cm maximum we recommend for employing the $Q_1(0)+S_0(0)$ transition, we adopt the value derived from the $S_1(0)+S_0(0)$ feature, along with the more conservative 95 % confidence limits. Finally, applying the apparatus-dependent Eqn. (16) yields the thickness of the doped front-side sample: $d_{front} = 0.136 \pm 0.007$ cm.

The gas-phase value[52,53] of the integrated molecular absorption coefficient for the ν_3 mode of CO_2 is $\int \alpha_{\nu 3\, CO2}(\tilde{\nu})\, d\tilde{\nu} = 5.49(0.21)\text{x}10^7$ cm/mol; including the Polo-Wilson factor for solid pH_2 from Eqn. (6) yields a corrected value of $5.82(0.22)\text{x}10^7$ cm/mol. Thus, the absolute $^{12}C^{16}O_2$ concentration calculated using Eqn. (3) is $C_{CO2} = 4.9(0.3)\text{x}10^{-8}$ mol/cm^3 (95 % confidence); Eqn. (5) yields a fractional concentration of $^{12}C^{16}O_2 = 1.13 \pm 0.07$ ppm, in good agreement with the 1.2 ppm value estimated from the inlet gas quantities of 0.11 μmol CO_2 and 95 mmol pH_2. The major contributors to the uncertainty in the CO_2 concentration are the sample thickness (5 %) and the literature value for the integrated absorption coefficient (4 %).

Similarly, we can estimate the concentrations of the other CO_2 isotopomers as: $^{13}C^{16}O_2 = 0.013 \pm 0.003$ ppm and $^{12}C^{16}O^{18}O = 0.003 \pm 0.002$ ppm. Thus, under these experimental conditions, we can estimate the detection limit for CO_2 molecules in a ≈ 0.1 cm-thick pH_2 solid as ≈ 0.003 ppm, with S:N $\approx$ 3:1. Employing the more sensitive InSb detector at an appropriately higher resolution would extend this limit to below ~ 0.001 ppm, which is comparable to the state-of-the-art for MIS studies on doped RGS hosts deposited within an integrating sphere.[15]

Combining the use of a pH_2 host with the integrating sphere geometry should yield even lower detection limits.

IV. SUMMARY

Rapid vapor deposited pH_2 solids offer a number of advantages as hosts for quantitative IR absorption spectroscopy. In particular, the sample thickness can be easily determined from the observed absorption intensities of the pH_2 host $Q_1(0)+S_0(0)$ and $S_1(0)+S_0(0)$ double transitions. Tables I and II summarize our recommended values for the integrated absorption intensities of these two bands, which we calibrate against interfererometrically determined sample thicknesses. Careful evaluation of the spectrometeric errors in our apparatus encourages our belief that our new values are more reliable than those published previously. Application of Beer's Law to data obtained from a ≈ 0.1 cm-thick CO_2/pH_2 sample demonstrates our ability to detect trapped CO_2 molecules at concentrations of a few parts-per-billion .

ACKNOWLEDGEMENTS

We thank Dr. C.W. Larson and Dr. A. Alfano for their critical readings of this manuscript and helpful suggestions.

REFERENCES

1. M.E. Fajardo and S. Tam, J. Chem. Phys. **108**, 4237 (1998).

2. S. Tam and M.E. Fajardo, Rev. Sci. Instrum. **70**, 1926 (1999).

3. S. Tam, M. Macler, and M.E. Fajardo, J. Chem. Phys. **106**, 8955 (1997).

4. S. Tam, M.E. Fajardo, H. Katsuki, H. Hoshina, T. Wakabayashi, and T. Momose, J. Chem. Phys. **111**, 4191 (1999).

5. N. Sogoshi, Y. Kato, T. Wakabayashi, T. Momose, S. Tam, M.E. DeRose, and M.E. Fajardo, J. Phys. Chem. A **104**, 3733 (2000).

6. S. Tam, M. Macler, M.E. DeRose, and M.E. Fajardo, J. Chem. Phys. **113**, 9067 (2000).

7. S. Tam and M.E. Fajardo, Low Temp. Phys. **26**, 653 (2000), [Fiz. Nizk. Temp. **26**, 889 (2000)].

8. M.E. Fajardo and S. Tam, J. Low Temp. Phys., accepted (2000).

9. M.R. Berman, editor, Proceedings of the High Energy Density Matter (HEDM) Contractors' Conference held 8-10 June 1999 in Cocoa Beach, FL, (U.S. Air Force Office of Scientific Research, Arlington, VA, 2000).

10. T. Oka, Annu. Rev. Phys. Chem. **44**, 299 (1993).

11. D.P. Weliky, K.E. Kerr, T.J. Byers, Y. Zhang, T. Momose, and T. Oka, J. Chem. Phys. **105**, 4461 (1996).

12. T. Momose and T. Shida, Bull. Chem. Soc. Jpn. **71**, 1 (1998).

13. T. Miyazaki, H. Tsuruta, and K. Fueki, J. Phys. Chem. **87**, 1611 (1983).

14. P.R. Griffiths and J.A. de Haseths, Fourier Transform Infrared Spectrometry, (Wiley, New York, 1986); see chapter 10.

15. Y. Ogawara, A. Bruneau, and T. Kimura, Anal. Chem. **66**, 4354 (1994).

16. W.B. Person, S.K. Rudys, and J.H. Newton, J. Phys. Chem. **79**, 2525 (1975).

17. R.C. Hilborn, Am. J. Phys. **50**, 982 (1982); erratum: Am. J. Phys. **51**, 471 (1983).

18. I.F. Silvera, Rev. Mod. Phys. **52**, 393 (1980).

19. H.P. Gush, W.F.J. Hare, E.J. Allin, and H.L. Welsh, Can. J. Phys. **38**, 176 (1960).

20. J. Van Kranendonk, Can. J. Phys. **38**, 240 (1960).

21. J. Van Kranendonk and H.P. Gush, Phys. Lett. **1**, 22 (1962).

22. J. Van Kranendonk and G. Karl, Rev. Mod. Phys. **40**, 531 (1968).

23. J. Van Kranendonk, Solid Hydrogen (Plenum Press, New York, 1982).

24. K.N. Rao, J.R. Gaines, T.K. Balasubramanian, and R.D. D'Cunha, Acta Physica Hungarica **55**, 383 (1984).

25. Q. Ma, R.H. Tipping, and J.D. Poll, Phys. Rev. B **39**, 132 (1989).

26. T.K. Balasubramanian, R. D'Souza, R.D. D'Cunha, and K.N. Rao, J. Mol. Spec. **153**, 741 (1992).

27. A. Nucara, P. Calvani, S. Cunsolo, S. Lupi, and B. Ruzicka, Phys. Rev. B **47**, 2590 (1993).

28. M. Mengel, B.P. Winnewisser, and M. Winnewisser, J. Mol. Spec. **188**, 221 (1998).

29. N.Q. Chako, J. Chem. Phys. **2**, 644 (1934).

30. S.R. Polo and M.K. Wilson, J. Chem. Phys. **23**, 2376 (1955).

31. J. Van Kranendonk, Physica **23**, 825 (1957).

32. W.B. Person, J. Chem. Phys. **28**, 319 (1958).

33. A.D. Buckingham, Proc. Roy. Soc. **A248**, 169 (1958).

34. P.N. Schatz, Spectrochimica Acta **21**, 617 (1965).

35. R.L. Fulton, J. Chem. Phys. **61**, 4141 (1974).

36. J.W. Warner and M. Wolfsberg, J. Chem. Phys. **78**, 1722 (1983).

37. J.E. Bertie and C.D. Keefe, J. Chem. Phys. **101**, 4610 (1994).

38. H.M. Roder, G.E. Childs, R.D. McCarty, and P.E. Angerhofer, Survey of the Properties of the Hydrogen Isotopes Below Their Critical Temperatures, NBS-TN-641, (U.S. Department of Commerce, Springfield, VA, 1973).

39. B.A. Wallace, Jr., and H. Meyer, J. Low Temp. Phys. **15**, 297 (1974).

40. P.C. Souers, Hydrogen Properties for Fusion Energy, (University of California Press, Berkeley, 1986).

41. B. Sonntag, "Dielectric and Optical Properties," in Rare Gas Solids Vol. II, edited by M.L. Klein and J.A. Venables, (Academic, London, 1977).

42. R.S. Mulliken, Phys. Rev. **36**, 611 (1930); we adapt the standard spectroscopic notation "$L_v(J)$" for rovibrational transitions of pH_2 molecules to vibrational level v, originating from v = 0 and rotational level J, with L = Q, S, and U for $\Delta J = 0, +2$, and $+4$, respectively.

43. F.L. Pedrotti and L.S. Pedrotti, Introduction to Optics, (Prentice-Hall, Englewood Cliffs, NJ, 1987).

44. M. Born and E. Wolf, Principles of Optics, (Pergamon, Oxford, 1980).

45. T. Hirschfeld, Anal. Chem. **51**, 495 (1979).

46. H. Ashkenas and F.S. Sherman, "Experimental Methods in Rarefied Gas Dynamics," in 4th International Symposium on Rarefied Gas Dynamics (Toronto), Vol. 2, edited by J.H. de Leeuw, (Academic, New York, 1966).

47. T. Hirschfeld, "Quantitative FT-IR: A Detailed Look at the Problems Involved," in

Fourier Transform Infrared Spectroscopy Vol. 2, edited by J.R. Ferraro and L.J. Basile, (Academic, New York, 1979).

48. D.B. Chase, Appl. Spectrosc. **38**, 491 (1984).

49. J.S. Wong, W.H. Green, Jr., C.K. Cheng, and C.B. Moore, J. Chem. Phys. **86**, 5994 (1987).

50. J. Mandel, The Statistical Analysis of Experimental Data, (Wiley, New York, 1964).

51. N.E. Holden, "Table of the Isotopes (Revised 1991)," in CRC Handbook of Chemistry and Physics 73rd Edition, D.R. Lide, editor (CRC Press, Boca Raton, FL, 1993).

52. M.A.H. Smith, C.P. Rinsland, B. Fridovich, and K.N. Rao, "Intensities and Collision Broadening Parameters from Infrared Spectra," in Molecular Spectroscopy: Modern Research Vol. III, K.N. Rao, editor (Academic, Orlando, FL, 1985).

53. V. Malathy Devi, B. Fridovich, G.D. Jones, and D.G.S. Snyder, J. Mol. Spec. **105**, 61 (1984).

TABLES

Table I. Summary of recommended values. We abbreviate $Q_1(0)+S_0(0)$ as "Q+S" and $S_1(0)+S_0(0)$ as "S+S." The stated uncertainties indicate the 95 % confidence limits.

Quantity	Recommended Value	Comments
n_{pH2}	1.14	refs. 38-40
$\int A_{Q+S} d\tilde{\nu} / \int A_{S+S} d\tilde{\nu}$	13.0 ± 0.4	this study
$\int A_{Q+S} d\tilde{\nu} / d_{total}$	82 ± 2 cm^{-2}	this study
$\int A_{S+S} d\tilde{\nu} / d_{total}$	6.3 ± 0.3 cm^{-2}	this study
d_{front}/d_{back}	11.5	apparatus specific

Table II. Comparision with literature values. We abbreviate $Q_1(0)+S_0(0)$ as "Q+S" and $S_1(0)+S_0(0)$ as "S+S." The stated uncertainties indicate the 95 % confidence limits.

Quantity	This Study	Literature	Comments
$<\tilde{\nu}>_{Q+S}$	4507 cm^{-1}		
$<\tilde{\nu}>_{S+S}$	4840 cm^{-1}		
$\alpha_{Q+S}/\alpha_{S+S}$	13.0 ± 0.4		
$\tilde{\alpha}_{Q+S}/\tilde{\alpha}_{S+S}$	14.0 ± 0.4	9.3	expt., refs. 19, 24
α_{Q+S}	189 ± 5 cm^{-2}		
α_{S+S}	14.5 ± 0.7 cm^{-2}		
$\tilde{\alpha}_{Q+S}$	4.84(±0.13)x10^{-14} cm^3/s	4.2x10^{-14} cm^3/s	expt., ref. 19
		4.5x10^{-14} cm^3/s	theory, ref. 20
$\tilde{\alpha}_{S+S}$	0.35(±0.02)x10^{-14} cm^3/s	0.45x10^{-14} cm^3/s	expt., ref. 24
		0.97x10^{-14} cm^3/s	theory, ref. 24
		0.56x10^{-14} cm^3/s	theory, ref. 26

FIGURE CAPTIONS

FIG. 1. Experimental Diagram.

FIG. 2. Test of Mattson FTIR spectrometer absorbance linearity. The inset shows the $\nu_1+\nu_4$ $CHCl_3$ absorption region for a nominal 5 % $CHCl_3/CCl_4$ solution at a pathlength of 0.573 cm. The top panel is a correlation plot of the integrated absorbance of this feature vs. sample pathlength, along with the best fit (unweighted least squares) straight line (dotted trace) and quadratic polynomial (solid trace). The bottom panel shows the residuals from the quadratic fit. The different symbols indicate successive experimental runs.

FIG. 3. Condensed phase induced features in the IR absorption spectrum of a vapor deposited pH_2 solid. The total (front + back) sample thickness is d_{total} = 0.11 cm; the sample was produced in a deposition time of t_{dep} = 0.5 hr using a pH_2 gas flow rate of Φ_{pH2} = 125 mmol/hr. The entire spectrum has been shifted vertically to yield zero absorbance at 4000 cm^{-1}. The dotted line segments indicate the baselines used for integration of the $Q_1(0)+S_0(0)$ (4495 to 4520 cm^{-1}) and $S_1(0)+S_0(0)$ (4825 to 4855 cm^{-1}) regions. The spectral resolution is 0.125 cm^{-1} FWHM.

FIG. 4. IR absorption spectra of a d_{total} = 0.038 cm thick pH_2 sample showing the variability of the $S_1(0)$ feature with sample history. Trace (a) is for the as-deposited sample at T = 2.3 K, trace (b) is the same sample warmed to T = 4.7 K, trace (c) cooled back down to T = 2.4 K. The spectral resolution is 0.09 cm^{-1} FWHM.

FIG. 5. Correlation plots of the integrated intensities of the $Q_1(0)+S_0(0)$ and $S_1(0)+S_0(0)$ features. Shown are data from 228 spectra of 90 different pure and doped ($C_{dopant} < 0.1$ %) samples at temperatures between 2 and 5 K. The various symbols indicate the spectral resolutions employed: open triangles 0.09 cm^{-1}, open circles 0.125 cm^{-1}, closed triangles 0.25 cm^{-1}, closed circles 1.0 cm^{-1}. The unweighted least-squares best fit straight line is constrained to pass through the origin ($y = a_1x$) and has a slope of $a_1 = 13.18$.

FIG. 6. Histogram of the quotient $\int A_{Q+S} d\tilde{\nu} / \int A_{S+S} d\tilde{\nu}$ for the same data depicted in Fig. 5. The solid curve is the normal distribution with the same mean ($\mu = 13.04$) and standard deviation ($\sigma = 1.22$) as the data.

FIG. 7. IR absorption spectra of three vapor deposited H_2 solids showing the evolution of the pattern of transmission interference fringes with increasing sample thickness. Trace (a) is for an Al/pH_2 sample with $d_{front} = 9.3$ μm, produced in $t_{dep} = 1.0$ hr using a pH_2 gas flow rate of $\Phi_{pH2} = 0.9$ mmol/hr. Trace (b) is for a B/pH_2 sample with $d_{front} = 34.3$ μm, and $d_{back} = 3.0$ μm, $t_{dep} = 1.0$ hr, and $\Phi_{pH2} = 2.6$ mmol/hr. Trace (c) is for a Na/pH_2 sample with $d_{back} = 32.5$ μm, $t_{dep} = 0.5$ hr, and $\Phi_{pH2} = 53$ mmol/hr. The atomic dopants are produced by pulsed laser ablation. The spectra are presented at 1 cm^{-1} FWHM resolution.

FIG. 8. Back-reflection HeNe laser interference fringes recorded during the deposition of a Si/pH_2 sample; $t_{dep} = 0.5$ hr, and $\Phi_{pH2} = 31$ mmol/hr. The inset shows the first two minutes of the deposition; the ratio of front:back fringes is roughly 11:1. The nearly 75 complete back side

fringes indicate that $d_{back} = 20.7$ μm.

FIG. 9. Correlation plot of $\int A_{Q+S} d\tilde{\nu}$ vs. d_{total} including data from all 11 samples for which both d_{front} and d_{back} can be determined directly from the transmission interference fringes in the IR spectra. The unweighted least-squares best fit straight line is constrained to pass through the origin ($y = a_1 x$) and has a slope of $a_1 = 0.00821$ $cm^{-1}/\mu m$.

FIG. 10. Extrapolation of the linear fit to $\int A_{Q+S} d\tilde{\nu}$ vs. d_{total}. The circles show the same data as in Fig. 9, for which both d_{front} and d_{back} are determined simultaneously. The squares show values of d_{total} estimated from d_{front}, and the triangles show values of d_{total} estimated from d_{back}, assuming a front:back thickness ratio of 11.5:1.

FIG. 11. IR absorption spectra of a natural isotopic abundance CO_2/pH_2 solid. Panel (a) shows the ν_3 transition of $^{12}C^{16}O_2$ while panel (b) shows the ν_3 transition of $^{13}C^{16}O_2$. The sample consists of 0.11 μmol CO_2 and 95 mmol pH_2 codeposited over a 0.5 hr period. The spectral resolution is 0.008 cm^{-1} FWHM.

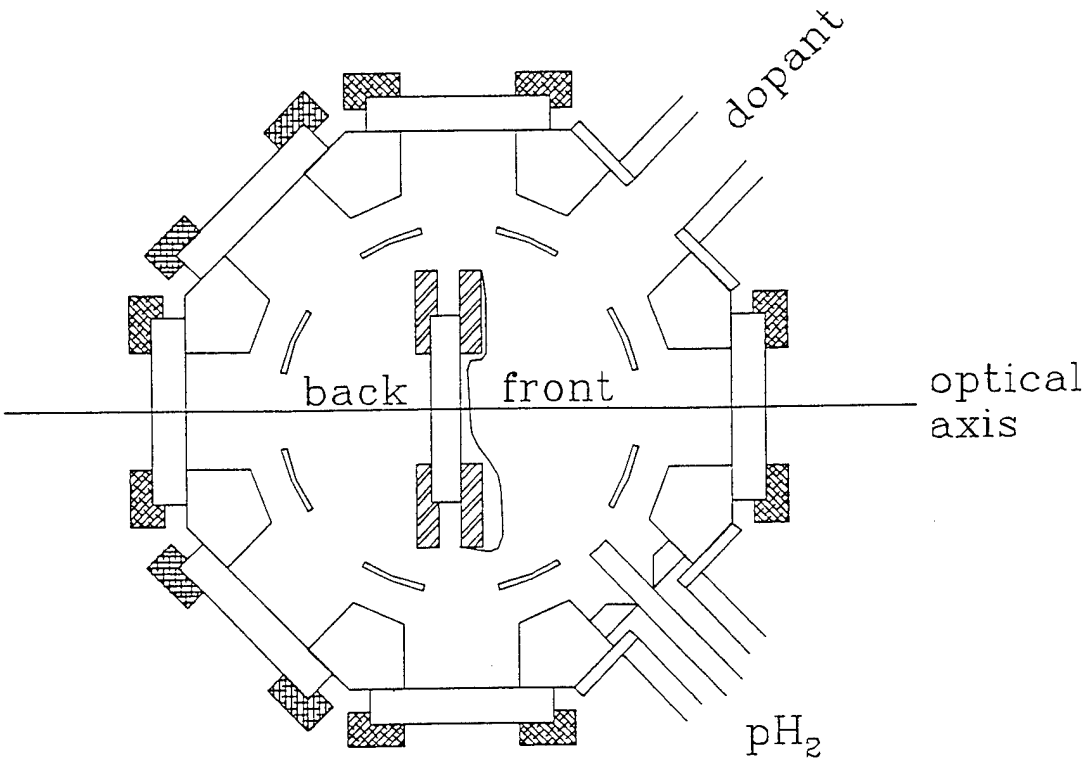

Fig. 1. Tam and Fajardo

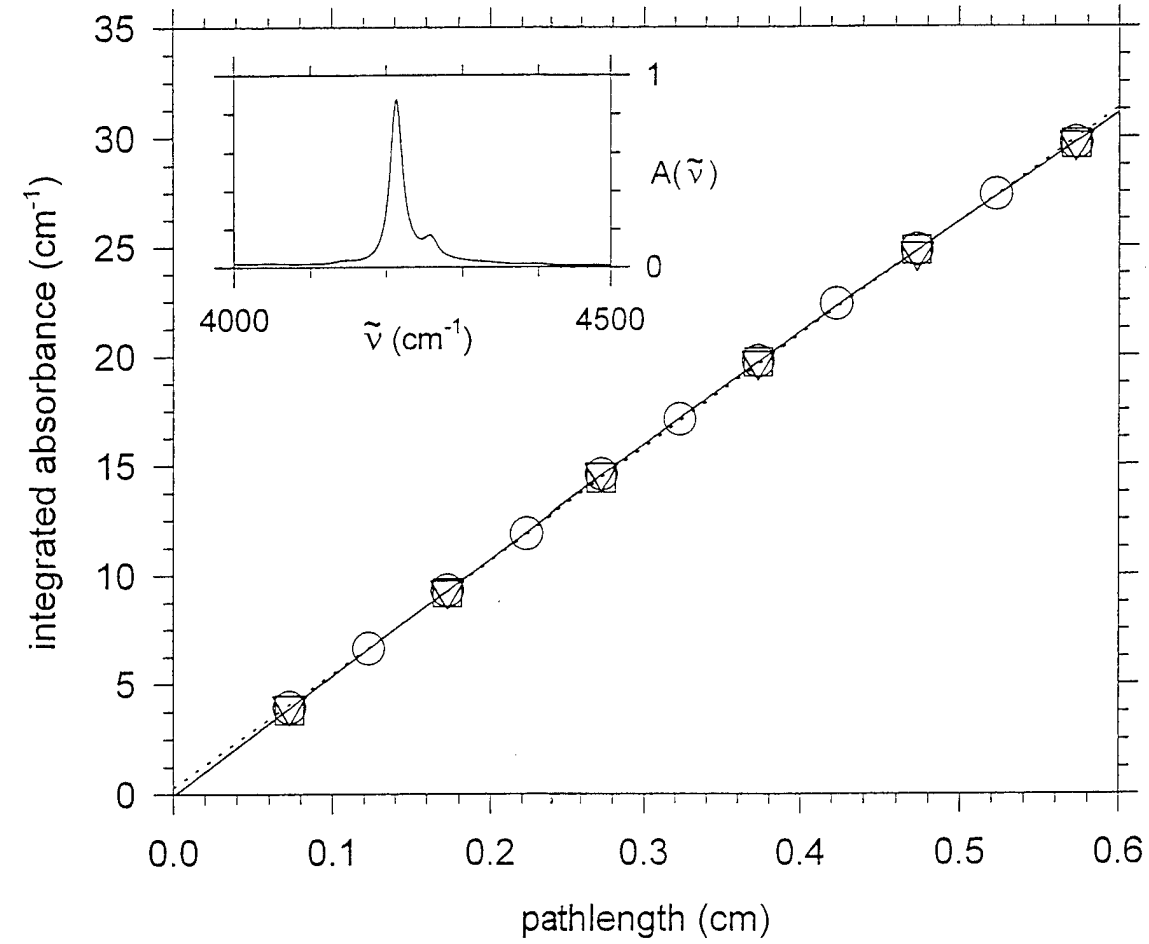

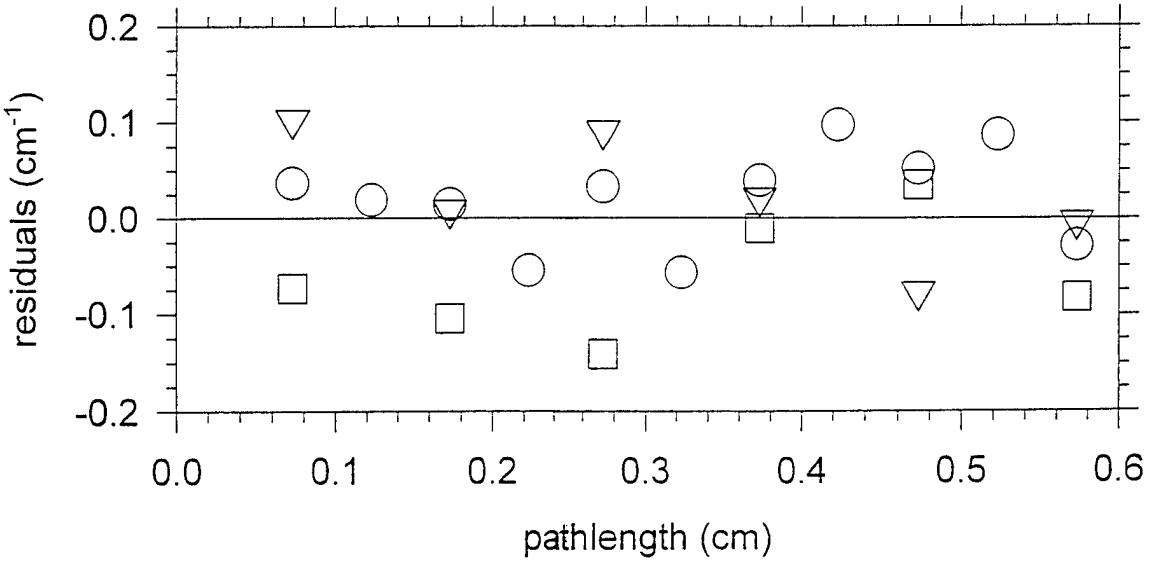

Fig. 2. Tam and Fajardo

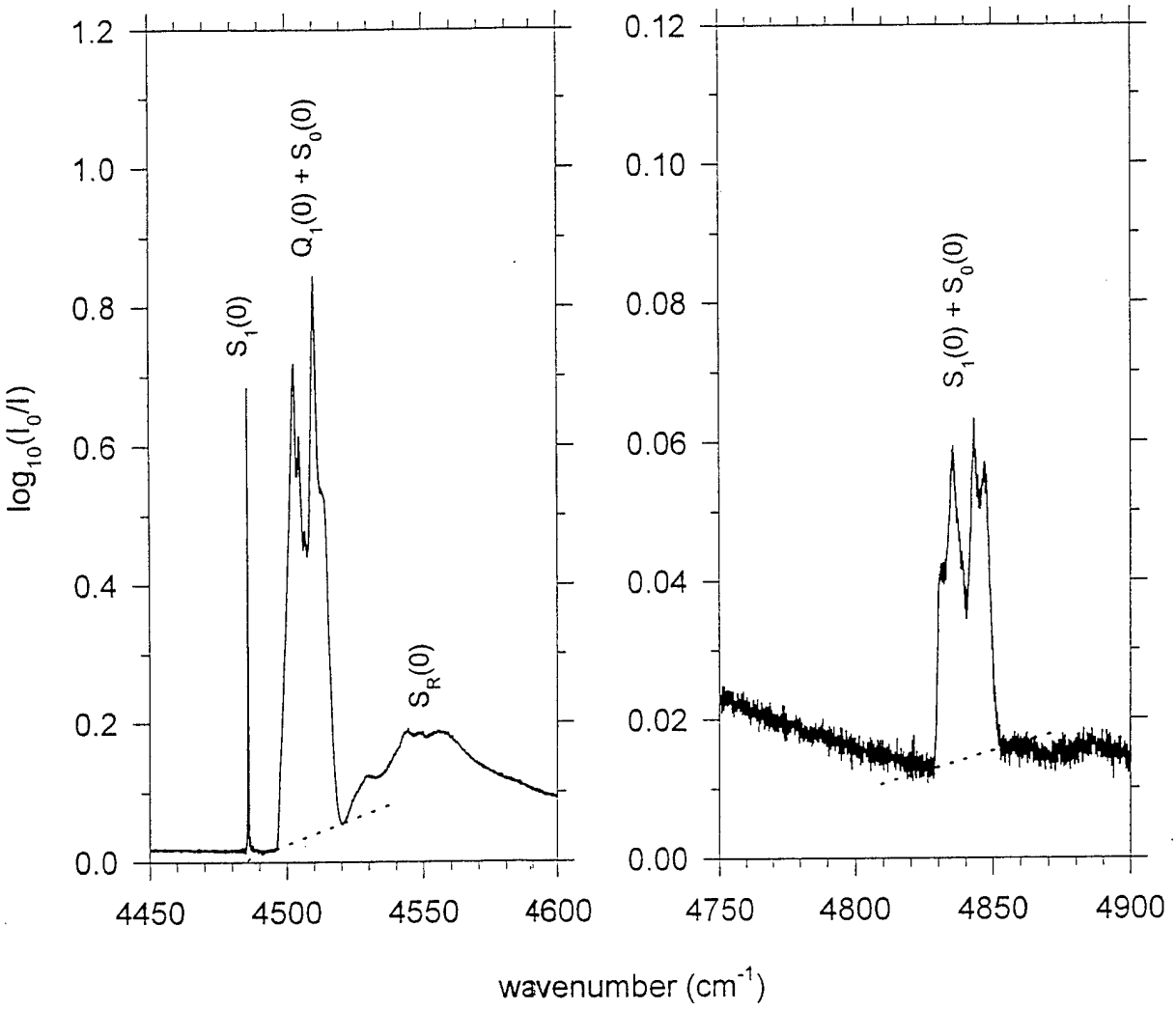

Fig. 3. Tam and Fajardo

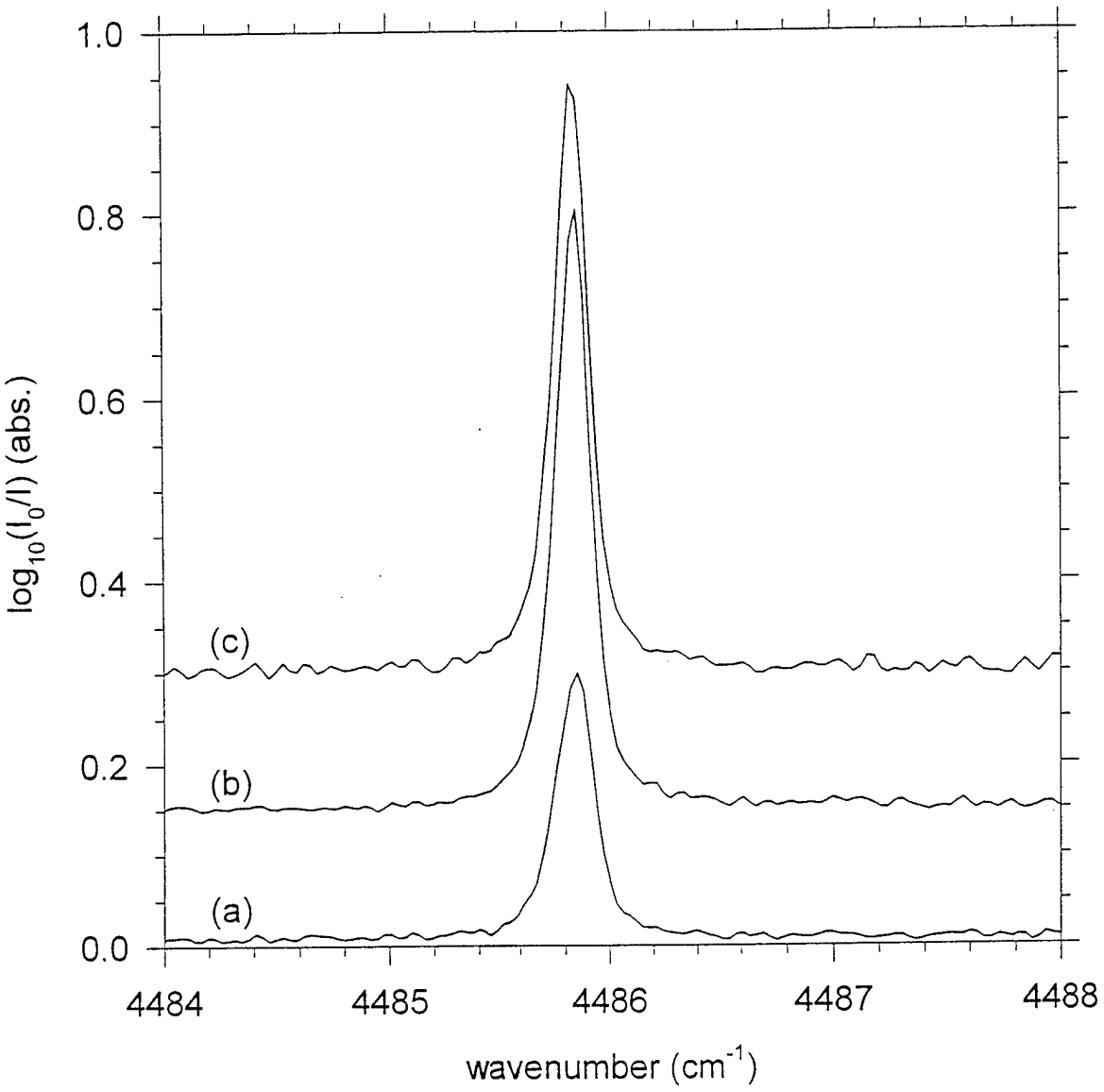

Fig. 4. Tam and Fajardo

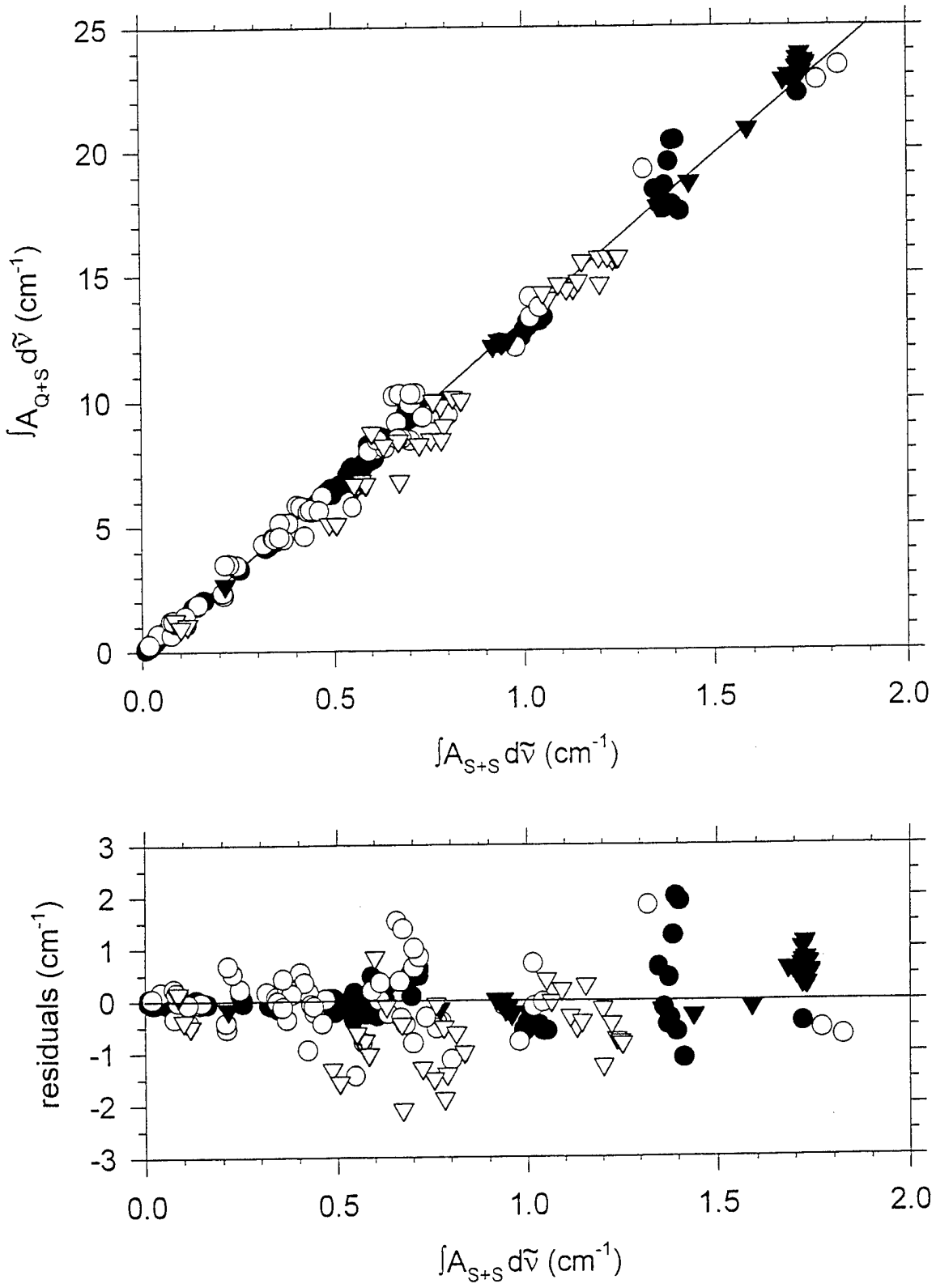

Fig. 5. Tam and Fajardo

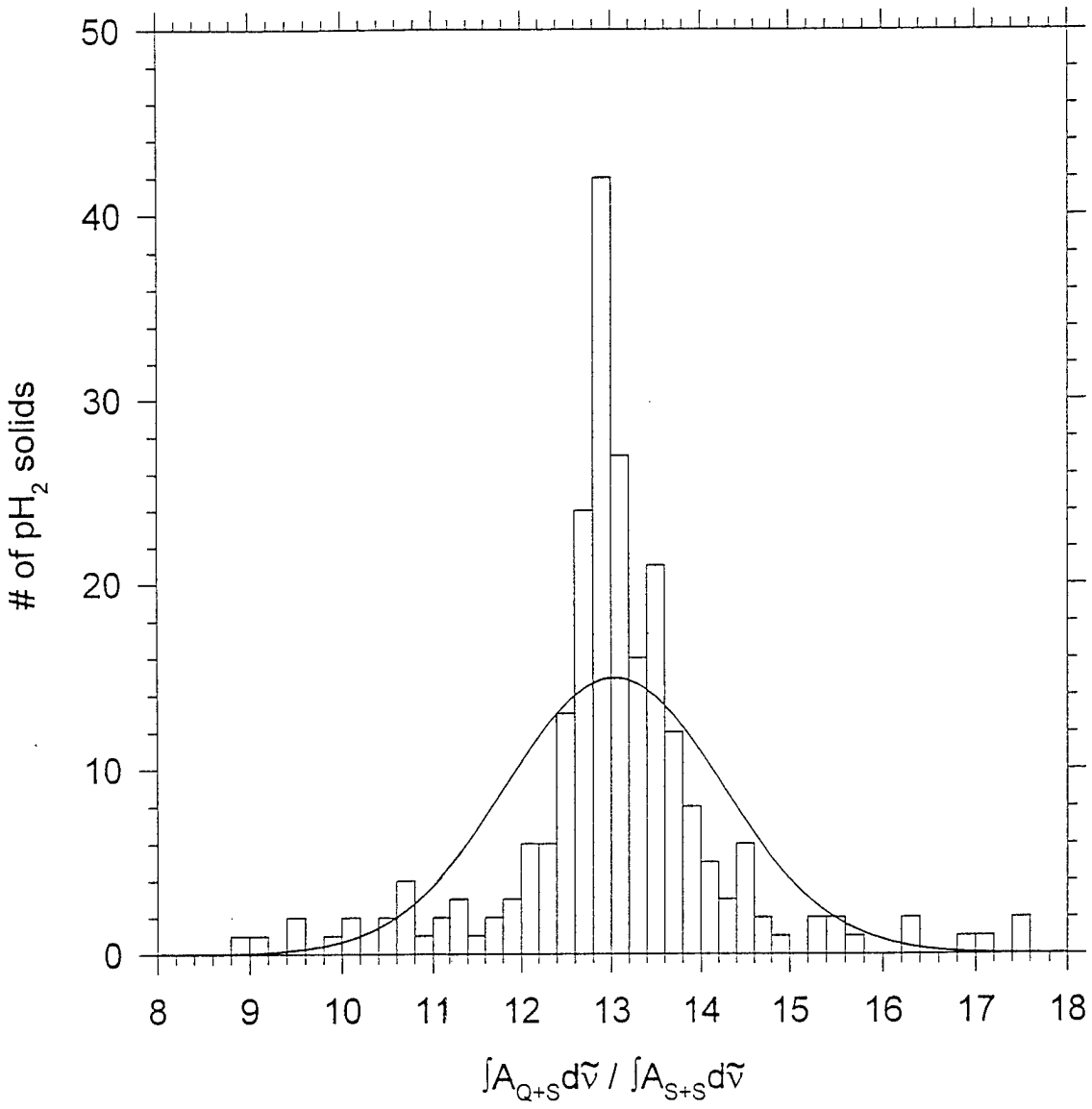

Fig. 6. Tam and Fajardo

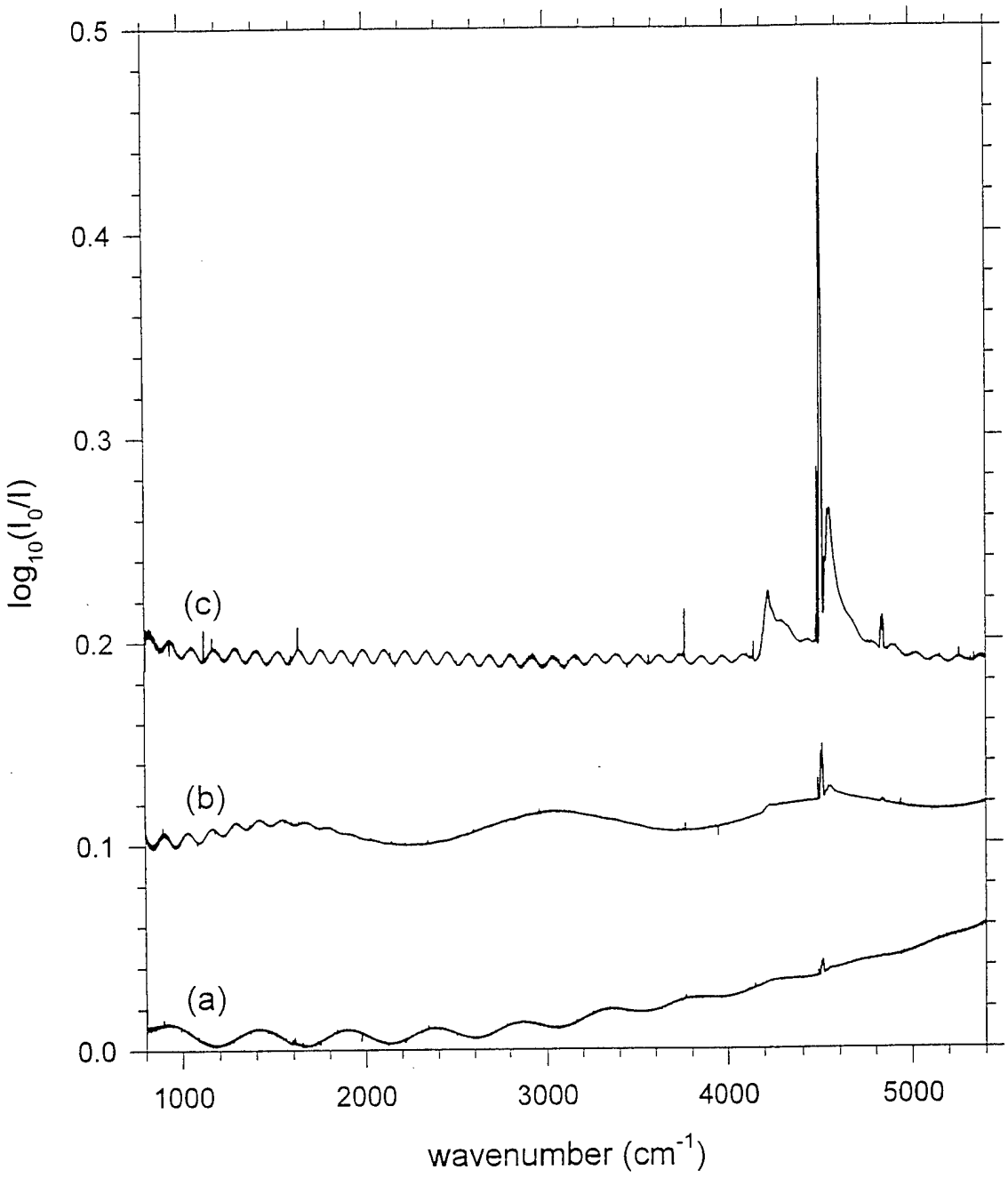

Fig. 7. Tam and Fajardo

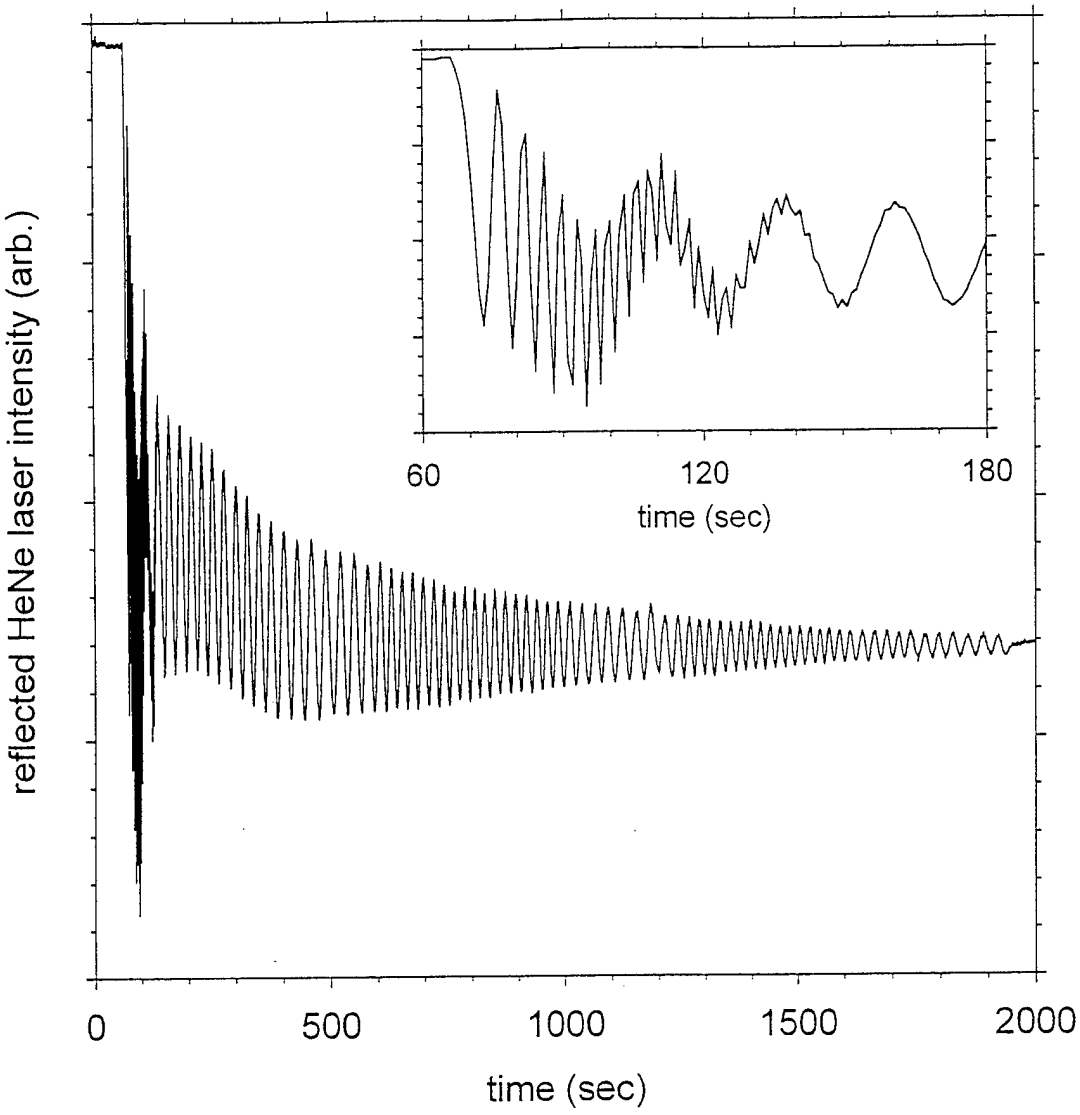

Fig. 8. Tam and Fajardo

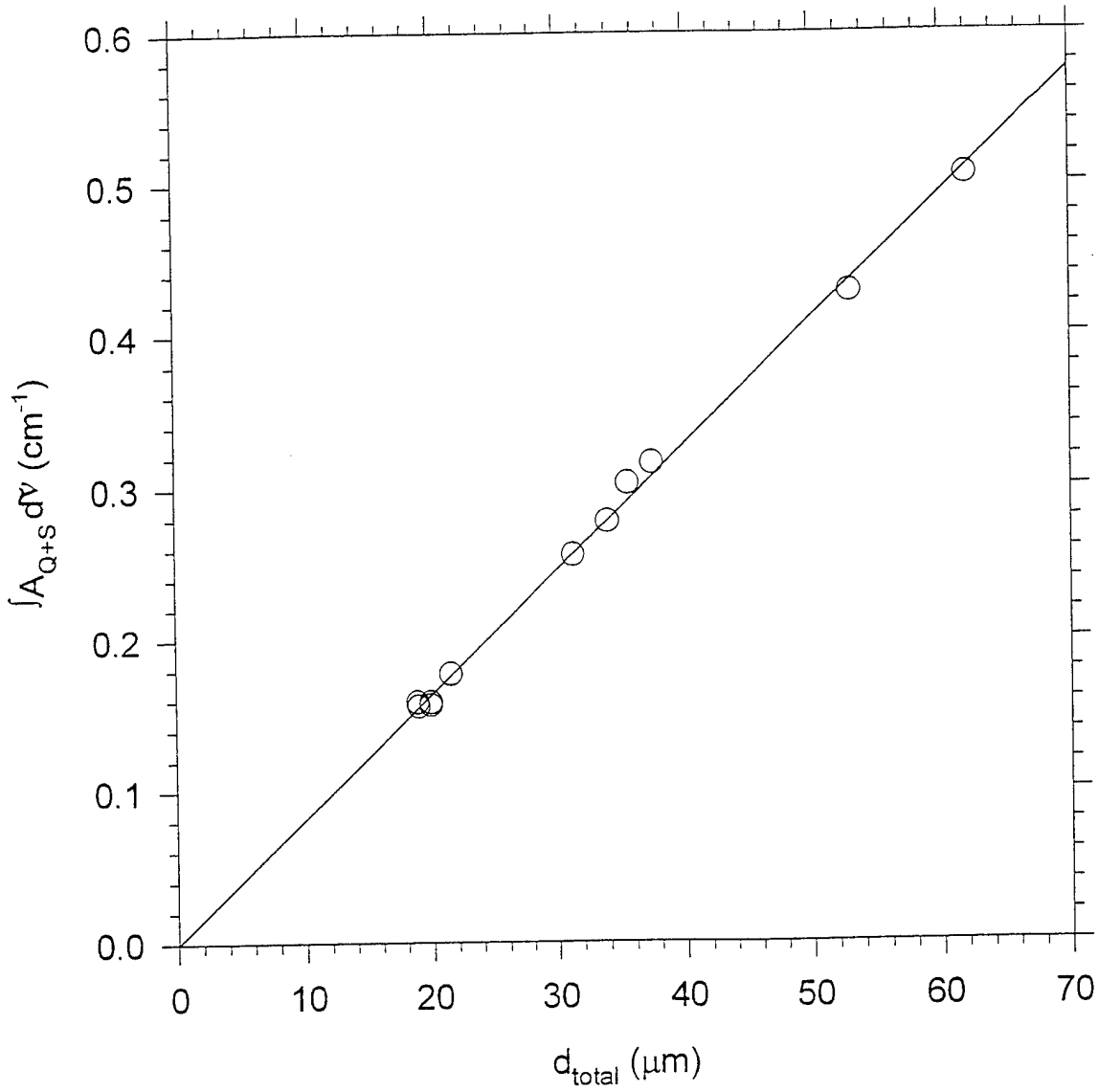

Fig. 9. Tam and Fajardo

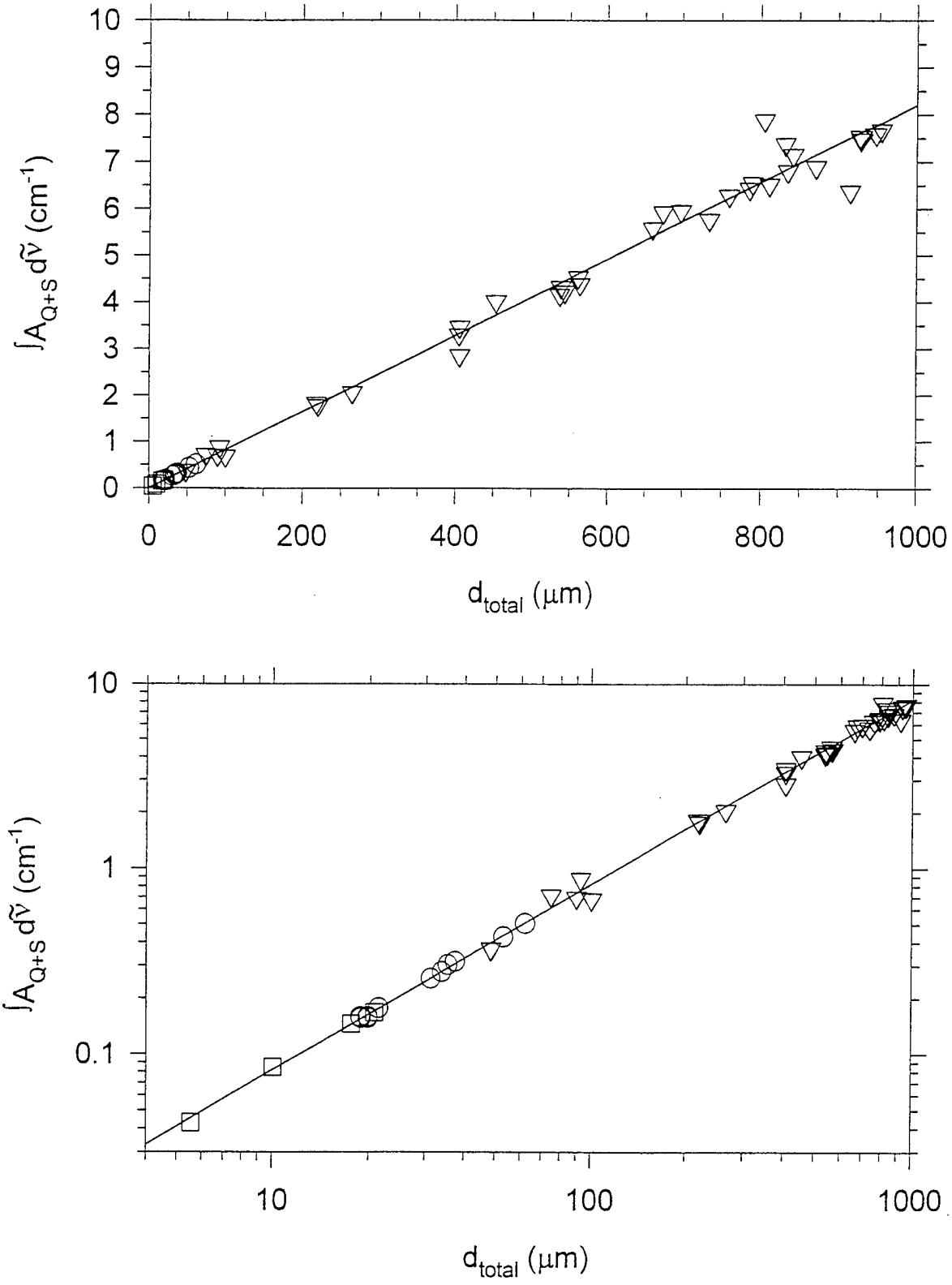

Fig. 10. Tam and Fajardo

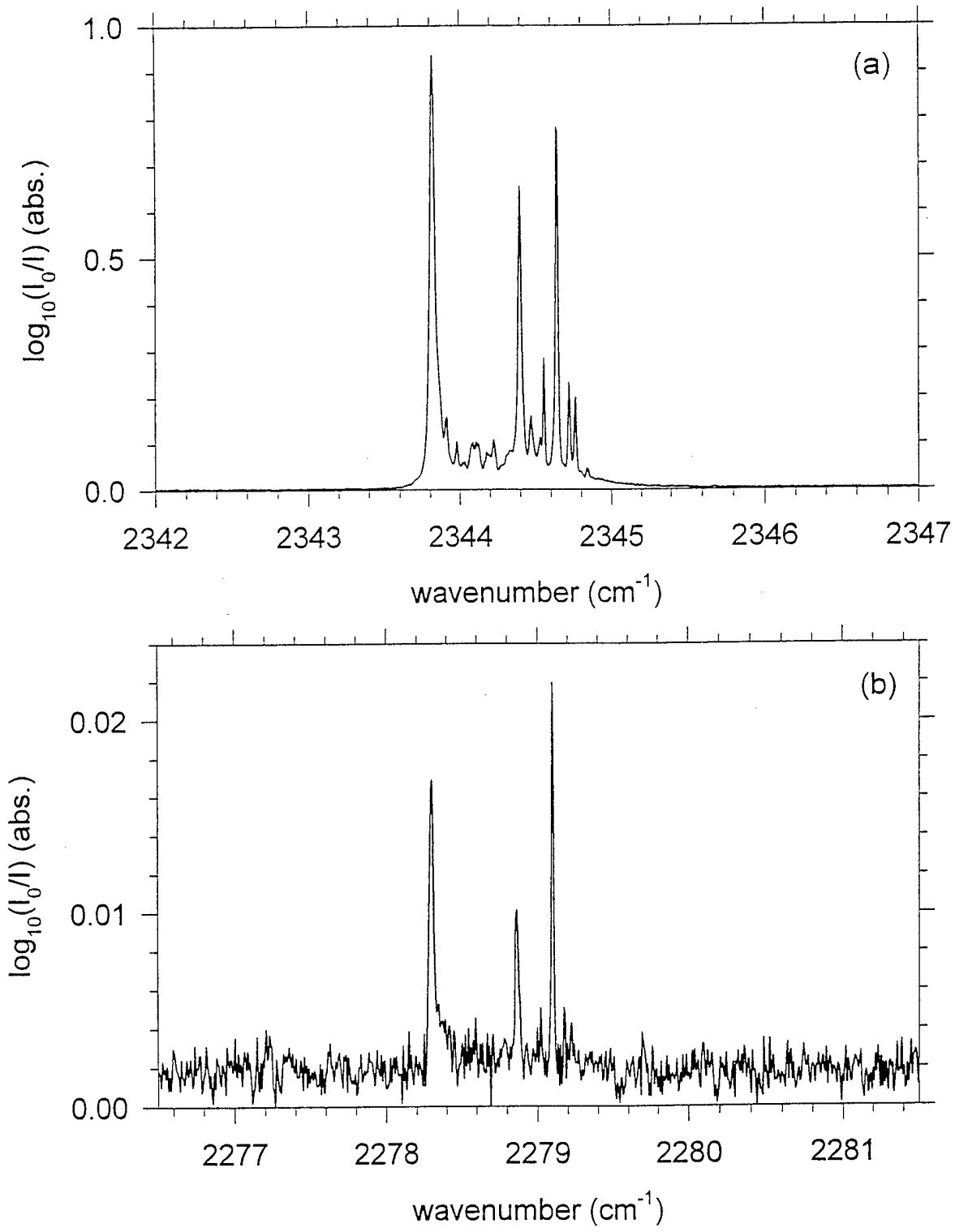

Fig. 11. Tam and Fajardo